Oral presentation | Fluid-structure interaction
Fluid-structure interaction-IV
Tue. Jul 16, 2024 10:45 AM - 11:45 AM Room A

[4-A-02] Fast and Robust Staggered Approach for Fluid-Structure Interaction Simulation in a Thin Flapping Plate

*Akio Yamano[1], Toshinobu Muramatsu[1], Takashi Iwasa[1] (1. Department of Aerospace Engineering, Graduate School of Engineering, Osaka Metropolitan University)

Keywords: Fluid-induced vibration, Vortex lattice method, Finite element method

**Twelfth International Conference on
Computational Fluid Dynamics (ICCFD12),
Kobe, Japan, July 14-19, 2024**

Fast and Robust Staggered Approach for Fluid–Structure Interaction Simulation in a Thin Flapping Plate

A. Yamano*, T. Muramatsu* and T. Iwasa*
Corresponding author: yamano_aero@omu.ac.jp
* Department of Aerospace Engineering, Graduate School of Engineering, Osaka Metropolitan University, Japan.

Abstract: This study reports the modeling and numerical simulations of the flow-induced vibration for a sheet under uniform flow, by considering the geometrical nonlinearity of sheet and wake shedding from the trailing edge. Then, in fluid–structure interaction (FSI) analysis using the sequentially staggered calculations, it has been reported that if the inertia force of the fluid force is dominant on the structure side, the interaction analysis becomes unstable (Artificial added mass instabilities). To avoid this instability problem, techniques such as the iterative staggered method, the added-mass compensation method, and so on are employed. In this study, we propose a FSI coupling method that does not require sub-iterations, has a lower computational cost, and is robust even under conditions where the inertia force of the fluid force is dominant.

Keywords: Fluid–structure Interaction, Computational Fluid Dynamics, Unsteady Problems.

1 Introduction

A "flutter-mill" is a micro wind energy harvesting device that uses sheet flapping and is a result of the interaction of a thin flexible sheet with an ambient fluid flow. Flutter-mills have gained popularity as a power source for sensors to monitor infrastructure and in IoT instruments that consume a small amount of electrical power. This is because the power generation device can be downsized more easily than conventional wind-power generators with lower manufacturing costs.

The power generation performance of the above-mentioned flutter mill depends on the specifications of the flexible flat plate employed and the inlet flow velocity, therefore, the preliminary evaluation during design with numerical analysis is important. To clarify these effects, Michelin et al. proposed a numerical model to survey the power generation performance for a small-span-width sheet in axial flow based on the slender body theory [1]. Separate studies by Alben and Shelley, Chen et al., and Michelin et al. also proposed the numerical model to reproduce the developed amplitude of the flapping oscillation under the assumption of two-dimensional potential flow for a fluid and the beam approximation for a sheet, respectively [2, 3, 4]. However, the slender-body theory and two-dimensional flow approximation for fluids are valid for a sheet with a specific span width. Moreover, the beam approximation for a sheet cannot reproduce the deformation along the span direction.

Computational fluid dynamics (CFD) analysis is more accurate than the above two approximations for fluid–structure interaction (FSI) analysis [5, 6, 7, 8, 9, 10, 11, 12, 13]. Tezduyar et al. and Sawada et al. employed the finite element modeling (FEM)-based FSI solver with a deformable mesh for the analysis of the flapping sheet [5, 6]. The combination of the lattice Boltzmann method (LBM) and immersed boundary method (IBM) were widely employed for the FSI analysis with a thin flexible sheet under a low Reynolds flow [7, 8, 9, 10]. Olivieri et al. reported the influence of grid-induced turbulence on the flapping sheet, through direct numerical simulation (DNS) with finite difference method (FDM) for fluid, spring-network structural model for structure, and IBM for coupling analysis [12]. Nawafleh et al. evaluated the flapping behavior of the sheet under laminar flow conditions by coupled analysis of a fluid model using a finite volume method with a structural grid and a structural model using a finite element method, using ANSYS FLUENT [13]. However, the choice of turbulence model, the number of divisions of the fluid and solid meshes, and the stability of the analysis must all be considered. Moreover, this method requires powerful computing resources.

This study reports the fast and robust FSI modeling and numerical simulations of the flow-induced vibration for a sheet under uniform flow, by considering the geometrical nonlinearity of the sheet. We

developed a numerical model to reproduce the large flapping behavior of a sheet while considering a span-wise deformation and three-dimensional (3D) fluid flow [14, 15]. Our approach modeled fluid flow using the unsteady vortex lattice method (UVLM) without the assumption mentioned above. This involves reduced computing costs compared to CFD analysis [16, 17, 18, 19]. A flexible sheet was modeled using the FEM with absolute nodal coordinate formulation (ANCF) for the shell element. This was done to reproduce the deformation of a plate while considering the span-wise deformation and geometrical nonlinearity [20, 21, 22].

Since the fluid and structural models are different, it is necessary to employ a sequential staggered procedure to solve this coupled system. In FSI analysis using the sequentially staggered calculations, however, it has been reported that if the inertia force of the fluid force is dominant on the structure side, the interaction analysis becomes unstable (Artificial added mass instabilities) [23]. FSI analysis whose the concerned solid for the application field is of large mass ratio; the aeroelastic analysis for wings [24, 25] etc., does not encounter this numerical instability. However, there is the case that the inertia force of the fluid force is dominant for the FSI problem for the thin flapping sheet [26, 27, 28].

Tang et al. proposed combining the fluid–structure strong coupled model with the nonlinear structure model and the linearized UVLM, with the combined model assuming that vortex panels are on a stationary plane to facilitate the construction of a strongly coupled model [29, 30]. Chen et al. and Luo et al. introduced sub-iterative calculations to improve accuracy and numerical stability in FSI models using nonlinear UVLM, respectively [31, 32]. However, the introduction of iterative calculations results in a large amount of computing time. Tang et al. and Zhang et al. employed the added-mass compensation method for the FSI model with beam structure model to stabilize the FSI analysis under the large inertia force of the fluid [27, 28]. The artificial added mass for stabilizing the numerical analysis is preferably a similar value to the added mass. However, the appropriate selection of the artificial added mass matrix for the shell structure model is more difficult than the beam structure model because there are many node variables for the shell element model.

In this study, therefore, we propose an FSI method that does not require sub-iterations, has a lower computational cost, and is robust even under conditions where the inertia force of the fluid force is dominant considering the nonlinearity of the large displacement of the sheet.

The remaining paper is organized as follows: In section 2, we propose the fast and robust FSI modeling of the flow-induced vibration for a sheet under uniform flow. In section 3, we verify our proposed numerical model comparatively with respect to existing literature, and confirm the effectiveness of the proposed numerical analysis method for the FSI modeling. Section 4 presents the conclusions of this study.

2 Problem Statement

2.1 Solid component

The proposed model is implemented based on the assumption that a flexible sheet with rectangular initial shapes is clamped at the leading-edge as shown in Fig. 1. Initially, the total length, width, and thickness of the sheet are set to L, H, and h, respectively. The sheet is situated in axial flow with an inlet flow velocity of U_∞.

We employ 36 d.o.f. absolute nodal coordinate formulation (ANCF) shell element of the finite element method (FEM), which is employed for the flexible multi-body dynamics analysis, to represent the kinematics of a sheet with large deformation [20]. In this reduced model, the dynamics of a sheet are represented by a position on the mid-surface. Subsequently, the position on the mid-surface is set to $\tilde{\boldsymbol{r}}$ and based on the assumption of Kirchhoff plate theory, the position $\boldsymbol{r}$ is decomposed as follows:

$$\boldsymbol{r}(\boldsymbol{x},t) = \tilde{\boldsymbol{r}}(x,y,t) + z\boldsymbol{n}(x,y,t), \tag{1}$$

where $\boldsymbol{n}(x,y,t)$ is the unit normal vector with respect to the mid-surface. The kinematics of the sheet considered in the proposed model were obtained using the principle of virtual work [22]:

$$\delta W_\mathrm{i} + \delta W_\mathrm{e} + \delta W_\mathrm{d} - \delta W_\mathrm{f} = 0, \tag{2}$$

where δW_i is the virtual work performed by the inertial force. δW_f is the virtual work done by the external force per unit volume $\boldsymbol{f}_\mathrm{ext}$ and pressure jump between each side of the sheet $[P] := P_\mathrm{L} - P_\mathrm{U}$, which is the difference between the pressure on the upper side P_U and lower side P_L. δW_e and δW_d are

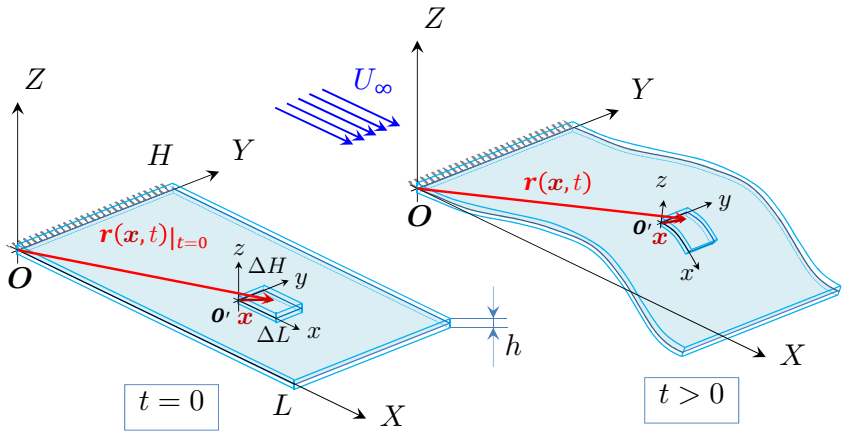

Figure 1: Flexible sheet in uniform flow. The total length, width, and thickness at the initial conditions were set to L, h, and h, respectively. U_∞ denotes the inlet flow velocity.

the virtual work terms corresponding to the internal elastic force and Kelvin-Voigt material damping force, which is proportional to the strain velocity, respectively.

The position $\tilde{\boldsymbol{r}}$ on an element can be expressed using the shape function $\boldsymbol{S}(x,y) \in \boldsymbol{R}^{3\times 36}$ and nodal coordinates $\boldsymbol{q} \in \boldsymbol{R}^{36}$ defined by Dufva and Shabana [20]:

$$\tilde{\boldsymbol{r}}(x,y,t) = \boldsymbol{S}(x,y)\boldsymbol{q}(t). \tag{3}$$

Then, the kinematics of each element is expressed as follows:

$$\boldsymbol{M}\mathrm{d}_t^2\boldsymbol{q} + \boldsymbol{Q}_{\mathrm{em}} + \boldsymbol{Q}_{\mathrm{e}\kappa} + \theta\left\{\boldsymbol{Q}_{\mathrm{dm}} + \boldsymbol{Q}_{\mathrm{d}\kappa}\right\} = \boldsymbol{Q}_{\mathrm{f}} + \boldsymbol{Q}_{\mathrm{ext}}, \tag{4}$$

where $\boldsymbol{M}$ is the mass matrix, $\boldsymbol{Q}_{\mathrm{em}}$, $\boldsymbol{Q}_{\mathrm{e}\kappa}$ are the membrane stiffness and bending stiffness vectors, $\boldsymbol{Q}_{\mathrm{dm}}$, $\boldsymbol{Q}_{\mathrm{d}\kappa}$ are the damping forces modeled using Kelvin–Voigt type material damping, and $\boldsymbol{Q}_{\mathrm{f}}$, $\boldsymbol{Q}_{\mathrm{ext}}$ are the fluid and body forces acting on the sheet [14, 15]. Then, θ is the structural damping parameter.

2.2 Nondimensionalization

The nondimensional parameters are introduced as follows:

$$\left.\begin{aligned}
&\tau := \frac{tU_\infty}{L},\ X^* := \frac{X}{L},\ Y^* := \frac{Y}{L},\ Z^* := \frac{Z}{L},\\
&x^* := \frac{x}{L},\ y^* := \frac{y}{L},\ z^* := \frac{z}{L},\ H^* := \frac{H}{L},\ h^* := \frac{h}{L},\\
&\mu := \frac{\rho_{\mathrm{m}} h}{\rho_{\mathrm{f}} L},\ \xi := \frac{EA}{\rho_{\mathrm{f}} LHU_\infty^2},\ \eta := \frac{EI}{\rho_{\mathrm{f}} L^3 HU_\infty^2},\\
&\theta^* := \frac{U_\infty\theta}{L},\ [p] := \frac{[P]}{\rho_{\mathrm{f}} U_\infty^2},\ \boldsymbol{f}_{\mathrm{ext}}^* := \frac{h}{\rho_{\mathrm{f}} U_\infty^2}\boldsymbol{f}_{\mathrm{ext}},
\end{aligned}\right\} \tag{5}$$

where ρ_{f} denotes the fluid density. The cross-sectional area A and second moment of area I of the sheet are represented by $A = Hh$ and $I = Hh^3/12$, respectively. θ^* is the material damping parameter nondimensionalized from θ.

Then, the non-dimensional kinematics of each element is expressed as follows [14, 15, 33]:

$$\mu\boldsymbol{M}^*\mathrm{d}_\tau^2\boldsymbol{q}^* + \xi\boldsymbol{Q}_{\mathrm{em}}^* + \eta\boldsymbol{Q}_{\mathrm{e}\kappa}^* + \theta^*\left\{\xi\boldsymbol{Q}_{\mathrm{dm}}^* + \eta\boldsymbol{Q}_{\mathrm{d}\kappa}^*\right\} = \boldsymbol{Q}_{\mathrm{f}}^* + \boldsymbol{Q}_{\mathrm{ext}}^*. \tag{6}$$

The kinematics of all the elements of the sheet are assembled from Eq. (6) which presents the kinematics for a single element:

$$\mu\boldsymbol{M}_{\mathrm{G}}^*\mathrm{d}_\tau^2\boldsymbol{q}_{\mathrm{G}}^* + \xi\boldsymbol{Q}_{\mathrm{em,G}}^* + \eta\boldsymbol{Q}_{\mathrm{e}\kappa,\mathrm{G}}^* + \theta^*\left\{\xi\boldsymbol{Q}_{\mathrm{dm,G}}^* + \eta\boldsymbol{Q}_{\mathrm{d}\kappa,\mathrm{G}}^*\right\} = \boldsymbol{Q}_{\mathrm{f,G}}^* + \boldsymbol{Q}_{\mathrm{ext,G}}^*, \tag{7}$$

where the subscript $\cdot_{\mathrm{G}}$ represents the vector or matrix after all the kinematics for each element are

assembled and $\boldsymbol{q}^*_{\mathrm{G}} \in \boldsymbol{R}^{N_{q\mathrm{G}}}$ is the assembled nodal coordinate.

2.3 Fluid component

The unsteady vortex lattice method (UVLM) is employed to model the airflow around the flexible sheet under the assumption of unsteady three-dimensional potential flow [16].

For the UVLM analysis, the leading segment of the vortex lattice is placed on the quarter-chord line of a plate element while the collocation point is at the center of the three-quarter chord line as shown in Fig. 2 [16, 17].

The nondimensionalized collocation point $\boldsymbol{r}^*_{\mathrm{c},i} := \boldsymbol{r}_{\mathrm{c},i}/L$ and nodes $\boldsymbol{r}^*_{\mathrm{p}m,i} := \boldsymbol{r}_{\mathrm{p}m,i}/L$ of the i-th vortex panel are defined as follows:

$$\boldsymbol{r}^*_{\mathrm{c},i} := \boldsymbol{S}^*_{\mathrm{c},i}\boldsymbol{q}^*,\ \boldsymbol{r}^*_{\mathrm{p}m,i} := \boldsymbol{S}^*_{\mathrm{p}m,i}\boldsymbol{q}^*,\ m = 1,2,3,4, \tag{8}$$

where $\boldsymbol{S}^*_{\mathrm{c},i}$ and $\boldsymbol{S}^*_{\mathrm{p}m,i}$, $i = 1,\ldots,n_{elem}$ are the nondimensionalized shape functions of the i-th vortex panel, which are defined to satisfy the one-quarter to three-quarters chord rule.

Owing to the no-penetration condition at the collocation point $\boldsymbol{r}^*_{\mathrm{c},i}$, the nondimensional circulations of the vortex lattices $\boldsymbol{\Gamma}^* = [\Gamma^*_i] := [\Gamma_i/LU_\infty] \in \boldsymbol{R}^{N_{\mathrm{elem}}}$ are obtained using the following system of linear equations:

$$\boldsymbol{A}\boldsymbol{\Gamma}^* = \boldsymbol{b}, \tag{9}$$

where $\boldsymbol{A} \in \boldsymbol{R}^{N_{\mathrm{elem}}\times N_{\mathrm{elem}}}$ and $\boldsymbol{b} \in \boldsymbol{R}^{N_{\mathrm{elem}}}$ are defined by

$$\boldsymbol{A} = [A_{ij}] := \left[\sum_{n=1}^{4} \boldsymbol{w}^{*T}_{n,ij}\boldsymbol{n}_i\right], \tag{10}$$

$$\boldsymbol{b} = [b_i] := \left[\left\{\mathrm{d}_\tau \boldsymbol{r}^*_{\mathrm{c},i} - U^*_\infty \boldsymbol{e}^*_X - \boldsymbol{u}^*_{\mathrm{wake}}(\boldsymbol{r}^*_{\mathrm{c},i})\right\}^T \boldsymbol{n}_i\right]. \tag{11}$$

Here, $\boldsymbol{w}^*_{n,ij}$ is the dimensionless velocity induced by the vortex lattice, which has a strength of Γ^*_j at a given collocation point $\boldsymbol{r}^*_{\mathrm{c},i}$. The vector $\boldsymbol{e}^*_X$ represents the unit basis along the X^* axis, while $\boldsymbol{u}^*_{\mathrm{wake}}(\boldsymbol{r}^*)$ is the flow velocity induced by the wake at position $\boldsymbol{r}^*$.

The nondimensionalized pressure jump between each side of the sheet $[p]$ is derived from the unsteady Bernoulli equation following the approach used by Katz and Plotkin [16]:

$$[p]_{kj} = [p]_{\mathrm{lift},kj} + [p]_{\mathrm{add},kj}, \tag{12}$$

$$[p]_{\mathrm{lift},kj} := \boldsymbol{V}^T_{\mathrm{surf},kj}\left\{\boldsymbol{\tau}_{x,kj}\frac{\Gamma^+_{k,j} - \Gamma^+_{k-1,j}}{\Delta L_{N_y(k-1)+j}} + \boldsymbol{\tau}_{y,kj}\frac{\Gamma^+_{k,j+1} - \Gamma^+_{k,j-1}}{2\Delta H_{N_y(k-1)+j}}\right\}, \tag{13}$$

$$[p]_{\mathrm{add},kj} := \mathrm{d}_\tau \Gamma^+_{k,j}, \tag{14}$$

$$\boldsymbol{V}_{\mathrm{surf},kj} := U^*_\infty \boldsymbol{e}^*_X + \left\{\sum_{j=1}^{N_{\mathrm{elem}}} \boldsymbol{u}^*_{\mathrm{ind},j}(\boldsymbol{r}^*) + \boldsymbol{u}^*_{\mathrm{wake}}(\boldsymbol{r}^*)\right\}\Bigg|_{\boldsymbol{r}^*=\tilde{\boldsymbol{r}}^*_{c,N_y(k-1)+j}} - \mathrm{d}_\tau \tilde{\boldsymbol{r}}^*_{c,N_y(k-1)+j}, \tag{15}$$

$$\Gamma^+_{kj} := \Gamma^*_{N_y(k-1)+j}, \tag{16}$$

where the subscript $\cdot_{kj}$ ($k = 1,\ldots,N_x$ and $j = 1,\ldots,N_y$) represents the value of the variable at the vortex lattice with the collocation point $\tilde{\boldsymbol{r}}^*_{c,N_y(k-1)+j}$.Furthermore, $\boldsymbol{\tau}_{x,kj}$ and $\boldsymbol{\tau}_{y,kj}$ are the unit tangential vectors along the x^* and y^* axes on the vortex lattice, respectively. The vector $\boldsymbol{u}^*_{\mathrm{ind},j}(\boldsymbol{r}^*)$ denotes the velocity at position $\boldsymbol{r}^*$, which is induced by the vortex lattices on the sheet.

In each time step for the numerical analysis, the vortex lattices in the wake are shed from the trailing edge of the sheet with a circulation strength that equals to the strength on the previous time step. These vortex lattices move with the local flow velocity [16, 19].

2.4 FSI coupling

We employed a sequentially staggered procedures to solve this coupled system. In FSI analysis using the sequentially staggered calculations, it has been reported that if the inertia force of the fluid force is dominant on the structure side, the interaction analysis becomes unstable (Artificial added mass

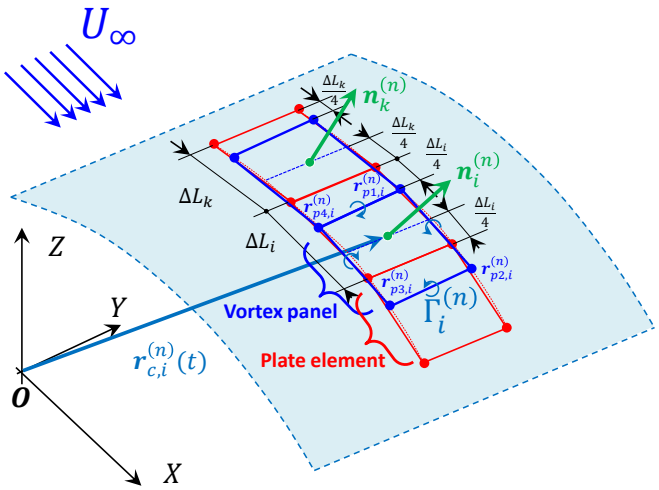

Figure 2: Vortex panels on the plate. Bound vortex panels are arranged to satisfy the 1/4–3/4 chord rule for a plate element in the ANCF analysis. The vector $\boldsymbol{r}_{\mathrm{c},i}$ is the collocation point of the i-th vortex panel, $\boldsymbol{r}_{\mathrm{p}m,i}$, $m = 1, 2, 3, 4$ are the positions of the nodes of the i-th vortex panel, Γ_i is the circulation strength of the i-th panel, and $\boldsymbol{n}_i$ is the unit normal vector of the i-th vortex panel.

instabilities) [23]. In this study, we propose an FSI method that does not require sub-iterations, has a lower computational cost, and is robust even under conditions where the inertia force of the fluid force is dominant.

Fig. 3 shows the mechanism of the artificial added mass instabilities under the sequential staggered FSI analysis with UVLM. In a coupled analysis using the sequential staggered method, there is a time delay of one-time step in the fluid forces acting on the structure. If the inertia force in the fluid force is dominant against the structural side, the term $[p]_{\mathrm{add}}$ in Eq. (12) leads to numerical instability. Therefore, we introduce a method to incorporate the term $[p]_{\mathrm{add}}$ of Eq. (12) into the structural model.

The term $[p]_{\mathrm{add},kj} = \mathrm{d}_\tau \Gamma^+_{k,j}$ in Eq. (12) is obtained from the time derivative of Eq. (9). Then,

$$\begin{aligned} (\mathrm{d}_\tau \boldsymbol{A})\,\boldsymbol{\Gamma}^* + \boldsymbol{A}\mathrm{d}_\tau \boldsymbol{\Gamma}^* &= \mathrm{d}_\tau \boldsymbol{b}, \\ \Leftrightarrow \mathrm{d}_\tau \boldsymbol{\Gamma}^* &= \boldsymbol{M}^*_{\mathrm{f1}} \mathrm{d}^2_\tau \boldsymbol{q}^*_{\mathrm{G}} + \boldsymbol{M}^*_{\mathrm{f2}}, \end{aligned} \tag{17}$$

where $\boldsymbol{M}^*_{\mathrm{f1}} \in \boldsymbol{R}^{N_{\mathrm{elem}} \times N_{q_{\mathrm{G}}}}$ and $\boldsymbol{M}^*_{\mathrm{f2}} \in \boldsymbol{R}^{N_{\mathrm{elem}}}$ are defined by

$$\boldsymbol{M}^*_{\mathrm{f1}} := \boldsymbol{A}^{-1} \left[\boldsymbol{n}_i^T \boldsymbol{S}^*_{\mathrm{c},i} \right]_{\mathrm{G}}, \tag{18}$$

$$\boldsymbol{M}^*_{\mathrm{f2}} := \boldsymbol{A}^{-1} \left\{ \left[-\mathrm{d}_\tau (\boldsymbol{u}^*_{\mathrm{wake}} (\boldsymbol{r}^*_{\mathrm{c},i})^T \boldsymbol{n}_i) + (\mathrm{d}_\tau \boldsymbol{r}^*_{\mathrm{c},i} - U^*_\infty \boldsymbol{e}^*_X)^T \mathrm{d}_\tau \boldsymbol{n}_i \right] - \mathrm{d}_\tau \boldsymbol{A} \cdot \boldsymbol{\Gamma}^* \right\}, \tag{19}$$

with the first term on the right-hand side of Eq. (17) representing the added-mass effect.

Fig. 4 shows the coupling procedure for the weak coupled analysis (above figure) and the proposed strongly coupled analysis (bottom figure) using the sequential staggered method. In the weak coupling, the strength of the circulation of the vortex lattice on the sheet is calculated using Eq. (9) from the positions of the sheet at the previous time step. Next, the fluid force acting on the sheet is calculated from Eq. (12) and solve the sheet kinematics using Eq. (6). On the other hand, Eqs. (18) and (19) are obtained using the UVLM solver in the proposed strong coupling. Next, we solve the sheet kinematics. The added-mass term calculated from the time derivative of Eq. (9) is then substituted on the left-hand side of Eq. (6) to compute the acceleration of the sheet directly as shown in Fig. 4. This approach reduces the computational cost compared to other methods that require numerous iterations to solve the FSI problem [34].

The flapping phenomenon behavior depends primarily on the three nondimensional parameters M^*, U^* and the aspect ratio H^*:

$$M^* := \frac{1}{\mu},\ U^* := \sqrt{\frac{\mu}{\eta}},\ H^* := \frac{H}{L}, \tag{20}$$

in which M^* represents the density ratio of for the fluid and the sheet, and U^* represents the free-stream velocity nondimensionalized by the sheet rigidity and inertia, which increases as the flow velocity

increases.

Fig. 5 shows comparisons of snapshot of flapping sheets (Fig. 5a) and computing time (Fig. 5b) among CFD analysis with Finite volume method (FVM) under full, half, and quarter fluid meshes and UVLM analysis in our model under $M^* = 1.0$, $H^* = 0.67$, $U^* = 15.5$ [33]. The thick lines highlighted in red represent the trailing edge displacement of the upper and lower sheets in the CFD analysis. Thin black and solid green lines represent the flapping behavior and instantaneous position of the sheets obtained from the proposed model, respectively. In addition, the proposed model reproduced CFD analysis. Moreover, as shown in Fig. 5b, the fluid analysis with UVLM achieved approximately 15 times faster than that CFD analysis with the full number of fluid meshes.

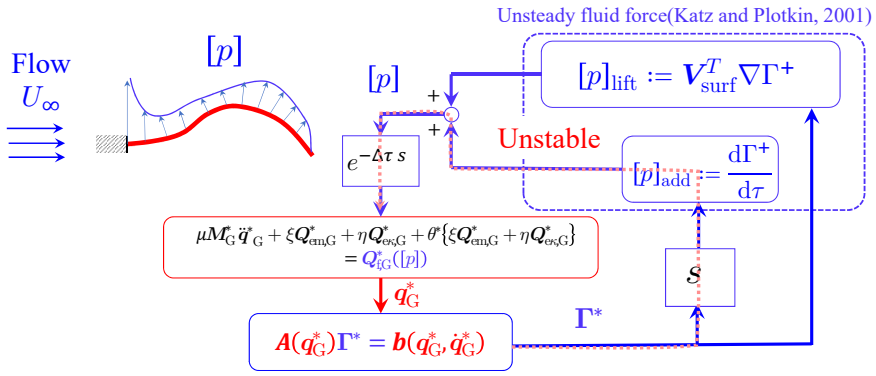

Figure 3: Artificial added mass instabilities under the sequential staggered FSI analysis with UVLM.

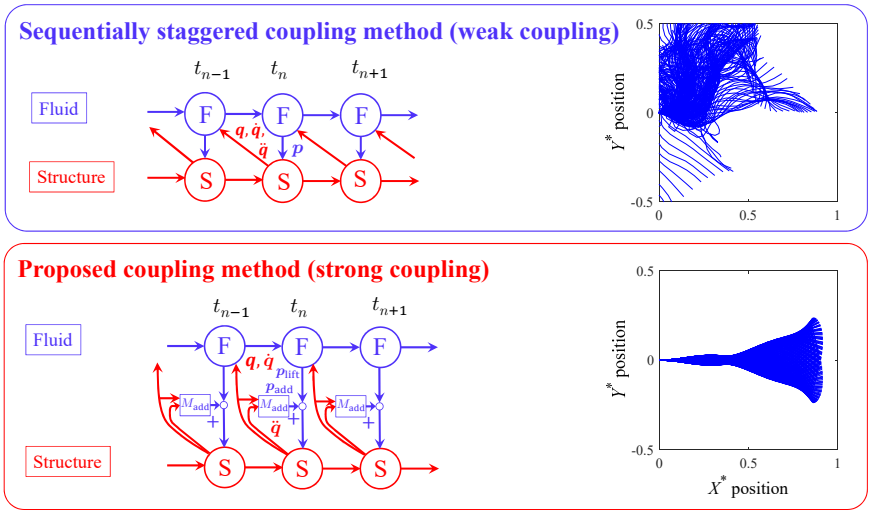

Figure 4: The idea of staggered strong-coupling FSI analysis. The right figures show the snapshots of a flapping sheet obtained under the fluid–structure coupling method shown in the left ($M^* = 2.0$, $W^* = 0.2$, $U^* = 20$).

Table 1: Specifications for computing machine [33].

CPU:	
Name	Ryzen 9 5900X (AMD, USA)
Clock	Base 3.7GHz, Max. 4.8GHz
Core number for analysis	4 Cores
Memory:	
Name	DDR4 AD4U3200732G22-D (ADATA, Taiwan)
Clock	3200MHz
Capacity	128GB

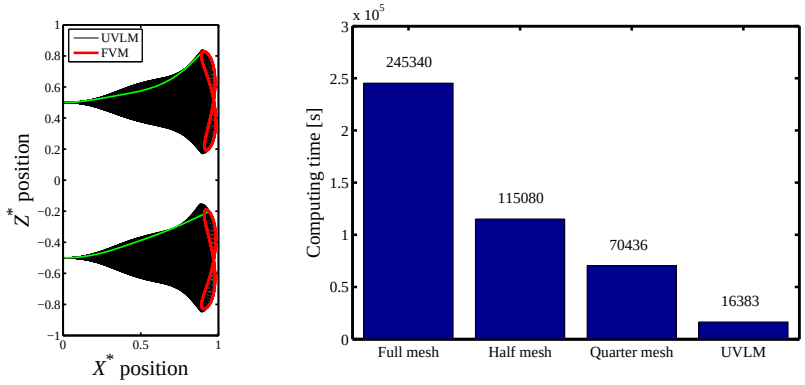

(a) Snapshot (b) Computing time

Figure 5: Comparisons of (a) snapshot and (b) computing time among CFD analysis with FVM under full, half, and quarter fluid meshes and UVLM analysis in our model under $M^* = 1.0$, $H^* = 0.67$, $U^* = 15.5$ [33].

Table 2: Parameters of the elastic plate [20].

		Case I (Dufva et al., 2005)
Young's modulus	E	1.0×10^5 Pa
Poisson's ratio	ν	0.3
Density	ρ_{m}	7810 kg/m^3
Length	L	0.3 m
Width	H	0.3 m
Thickness	h	0.01 m
Boundary condition		Spherical joint at the corner node

3 Results and Discussion

The validity and numerical stability of the constructed FSI model are confirmed. Then, the analysis was performed under the condition $\theta^* = 0$, where there is no structural damping.

3.1 Verifications of solid component

To verify the validity of the dynamic model of an elastic sheet constructed using ANCF shell elements, the constructed model is compared with the preceding study dealing with the free fall problem of an elastic sheet under the spherical joint boundary condition [20].

The parameters and specifications employed for the numerical analysis are listed in Table 2 and Table 3. Fig. 6a describes the behavior of the elastic sheet during free fall obtained under the analytical conditions shown in Table 2. Solid lines and dashed, chain lines shown in Fig. 6b show the comparisons of the time series of position at the selected point and the snapshot between the numerical result and the preceding report [20], respectively. Moreover, Fig. 6c shows the time series of each energy of the falling plate. The green solid line, red solid line, black dashed line, and magenta dashed line are the kinetic energy, potential energy by gravity, elastic energy of the membrane stiffness, and bending stiffness energy, respectively.

As shown in the time series of displacement of Fig. 6b, the numerical analysis results shown in solid lines is consistent with the reports of the preceding study as shown in dashed and chain lines. Moreover, we can confirm that the effect of numerical damping is small, as shown by the blue solid line indicating the sum of the energies in Fig. 6c.

3.2 Verifications of fluid component

To verify the fluid component based on the UVLM analysis, the lift coefficient C_L obtained by the UVLM is compared to Theodorsen's aerodynamics [35]. The lift coefficient C_L acting on the plate pitching at

Table 3: Parameters employed in the numerical analysis.

The number of element	N_{elem}	8×8
Step time	Δt	5.0×10^{-4} s
Analytical time	$t_{\max}$	1.0 s

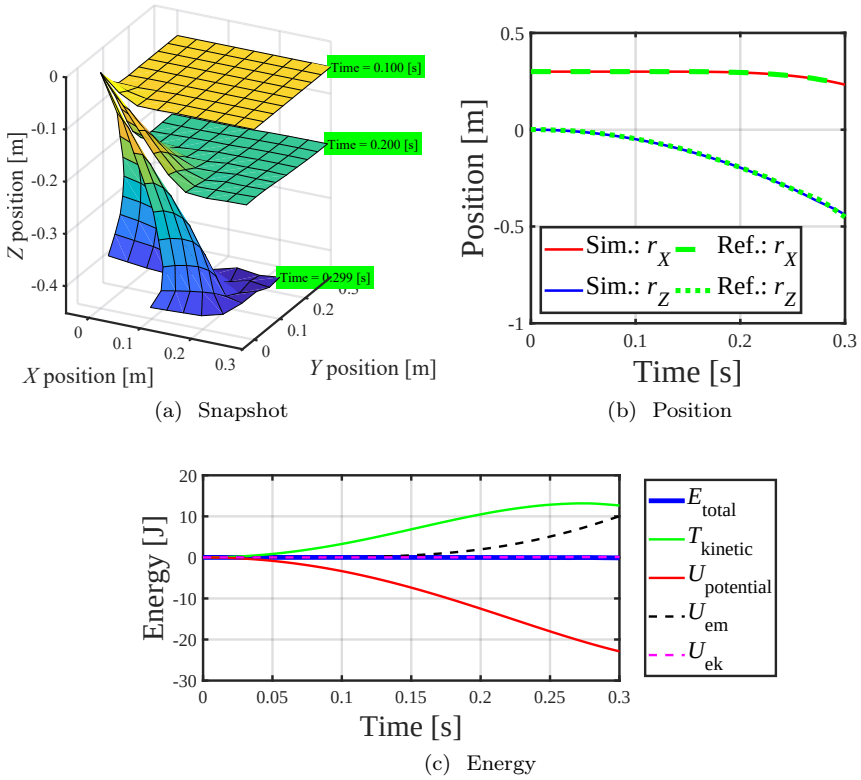

(a) Snapshot (b) Position

(c) Energy

Figure 6: (a) Snapshot, (b) the time series of behavior, and (c) energy of the flexible fall pendulum under Case I.

the half cord by the angle of attack $\alpha = \bar{\alpha}\sin(\omega^* \tau)$ is denoted by

$$C_L(\tau) = \mathrm{Im}\left(\pi\left\{(2+jk)C(k)+jk\right\}\bar{\alpha}e^{j\omega^*\tau}\right), \tag{21}$$

where $k := \omega^*/2$ is the reduced angular frequency, and $C(k)$ is the Theodorsen's function.

Fig. 7 shows comparisons of the lift coefficient C_L between the UVLM analysis and Theodorsen's solutions under reduced angular frequency: $k = 0.5$ and 1.0 and amplitude: $\bar{\alpha} = \pi/6$, $\pi/18$, $\pi/60$ [rad]. Blue lines show the lift coefficient obtained by UVLM analysis and red lines show the results by Eq. (21). Then, for the UVLM analysis, the analysis conditions in Table 4 were employed. The aspect ratio $H^* = 50$ is employed for UVLM analysis because Theodorsen's solution for the lift coefficient is obtained under the two-dimensional flow assumption. The pressure jump distribution $[p]$ at the mid-span was employed to calculate the lift coefficient from the UVLM analysis.

As shown in Fig. 7a, the discrepancy between the analytical solution in Eq. (21) and the numerical solution by UVLM is large under the large amplitude of pitching motion $\bar{\alpha}$. This is because the lift coefficient of Eq. (21) is obtained under the assumption of small amplitudes, and it can be seen that the discrepancy between the two is small when the pitch angle amplitude is small, as shown in Figs. 7b and 7c.

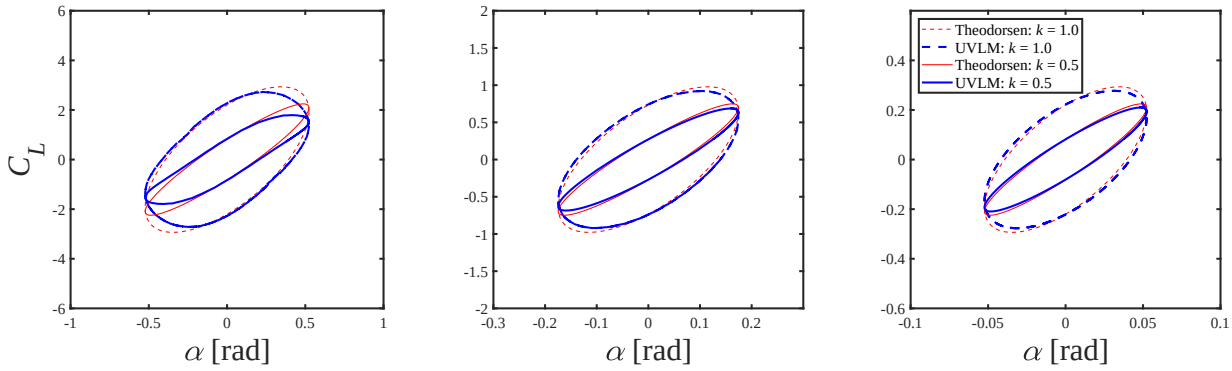

(a) $\bar{\alpha} = \pi/6$ [rad] (b) $\bar{\alpha} = \pi/18$ [rad] (c) $\bar{\alpha} = \pi/60$ [rad]

Figure 7: Comparisons of the lift coefficient C_L between the UVLM analysis and Theodorsen's solutions under reduced angular frequency: $k = 0.5$ and 1.0 and amplitude: $\bar{\alpha} = \pi/6,\ \pi/18,\ \pi/60$ [rad].

Table 4: Parameters employed in the numerical analysis.

The number of element	$N_x \times N_y$	14×40
Aspect ratio	H^*	50
Analytical time	$\tau_{\max}$	15

3.3 Stability comparisons

Fig. 8a shows the stability comparisons between the weak-coupling and the proposed strong-coupling FSI analysis. In the weak coupled analysis, $\mathrm{d}_\tau \Gamma^+_{k,j} \simeq \Delta\tau^{-1}\left\{\Gamma^{+(n)}_{k,j} - \Gamma^{+(n-1)}_{k,j}\right\}$ was employed to calculate Eq. (12). Blue markers show the results by the weak-coupling and red markers show the results by the proposed strong-coupling method. Fig. 8b shows the comparisons of the time series of displacement at the trailing edge of the mid-span width between the weak-coupling (red dotted line) and proposed strong-coupling (blue solid line) under the conditions $M^* = 1.5$, $U^* = 17$, $H^* = 1.0$.

As shown in Fig. 8a, when the mass ratio M^* and the aspect ratio H^* are large, the weakly coupled analysis using the sequential staggered method indicated by the blue markers does not converge as shown in the red dotted line of Fig. 8b. This is because, in FSI analysis using the sequentially staggered calculations, it has been reported that if the inertia force of the fluid force is dominant on the structure side, the interaction analysis becomes unstable (Artificial added mass instabilities) [23]. On the other hand, the proposed strong-coupling method achieved convergence without sub-iterations, even when the inertia force of the fluid force is dominant on the structure side. A comparison of the computational times of both coupled methods showed that the difference was less than 10 % as shown in Table 5.

Fig. 9 shows the flapping behavior comparisons of a flexible sheet at the mid-span width between the weak-coupling and proposed strong-coupling FSI analysis under $M^* = 0.4$, $U^* = 13$, $H^* = 1.0$ (Figs. 9a and 9e), $M^* = 0.5$, $U^* = 15$, $H^* = 0.5$ (Figs. 9b and 9f), $M^* = 1.0$, $U^* = 15$, $H^* = 0.3$ (Figs. 9c and 9g), and $M^* = 1.5$, $U^* = 17$, $H^* = 0.2$ (Figs. 9d and 9h).

As shown in Figs. 9a and 9e, there is the discrepancy at the trailing edge displacement between weak coupling and the proposed coupling analysis under a large aspect ratio. On the other hand, this discrepancy is small under a small aspect ratio as shown in Figs. 9b to 9h.

Figs. 10d and 11d show the velocity norm $|\boldsymbol{u}^*| = \sqrt{{u^*_{x^*}}^2 + {u^*_{z^*}}^2}$ distribution comparisons between the weak-coupling (top) and proposed strong-coupling FSI analysis (bottom) under $M^* = 0.4$, $U^* = 13$, $H^* = 1.0$ and $M^* = 1.5$, $U^* = 17$, $H^* = 0.2$, respectively. Then, when the period of vibration is defined as τ_p, the left figures ((a) and (c)) show the flow velocity distribution at the 0 period, and the right figures ((b) and (d)) show the flow velocity distribution at 1/4 of the period ($\tau_p/4$).

No significant difference is observed in the velocity distribution near the flapping sheet between the two coupling methods. In addition, as shown in Figs. 10, it can be seen that on the sheet and shear layer, the velocity difference between the top and bottom of the sheet and shear layer is large at the position with large curvature, which is similar to the experimental PIV observations [36].

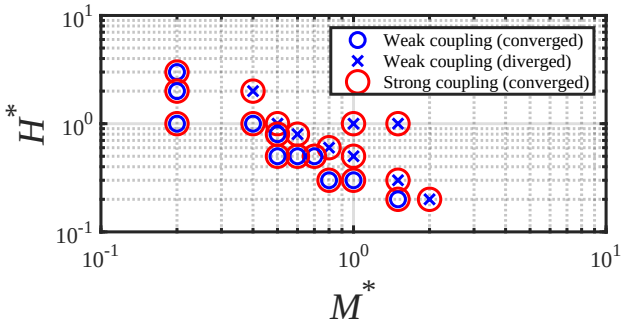

(a) Stability comparisons

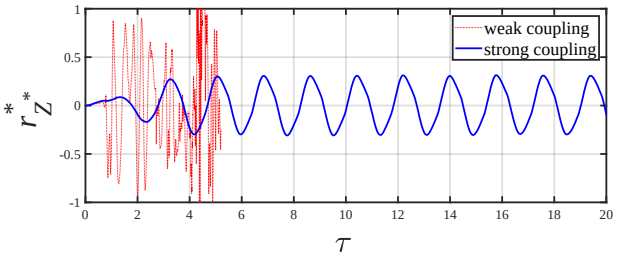

(b) Time series comparisons

Figure 8: Stability comparisons between the weak-coupling and proposed strong-coupling FSI analysis under (a) various mass ratio and aspect ratio, and (b) comparisons of the time series of displacement at the trailing edge between the weak-coupling and proposed strong-coupling under the conditions $M^* = 1.5$, $U^* = 17$, $H^* = 1.0$.

Table 5: Computing time ratio between the strong coupling and weak coupling FSI.

	$\tau_{\max}$	Strong coupling	Strong coupling / Weak coupling
$M^* = 0.2,\ U^* = 11,\ H^* = 3.0$	60	8.379×10^4 s	1.070
$M^* = 0.5,\ U^* = 15,\ H^* = 0.5$	40	3.894×10^4 s	1.039
$M^* = 1.0,\ U^* = 15,\ H^* = 0.3$	30	1.808×10^4 s	1.053
$M^* = 1.5,\ U^* = 17,\ H^* = 0.2$	30	2.239×10^4 s	1.045

4 Conclusion and Future Work

This study reported the fast and robust FSI interaction modeling and numerical simulations of the flow-induced vibration for a sheet under uniform flow, by considering the geometrical nonlinearity of the sheet. We proposed an FSI coupling method that does not require sub-iterations, has a lower computational cost, and is robust even under conditions where the inertia force of the fluid force is dominant. The results are summarized as follows:

1. In UVLM, the added mass term acting on the sheet can be calculated by time differentiating both sides of the linear equation obtained by the non-penetration condition at the collocation point.

2. By constructing a coupled model in which the added mass term is transferred to the structural model in the FSI analysis using the sequential staggered method, convergence is achieved in almost the same computation time as in the weak coupled analysis, even when the inertial force of the fluid force is dominant on the structure. A comparison of the computational times of both coupled methods showed that the difference was less than 10 %.

3. At the large aspect ratio of a flapping sheet, a discrepancy was observed in the displacement of the trailing edge of the sheet between the weakly coupled and the proposed coupled analyses, but this discrepancy became smaller at the small aspect ratio of the sheet.

A discrepancy was observed in the displacement of the trailing edge of the sheet at large aspect ratios between the weakly coupled and the proposed coupled FSI analyses. In addition, even in the proposed

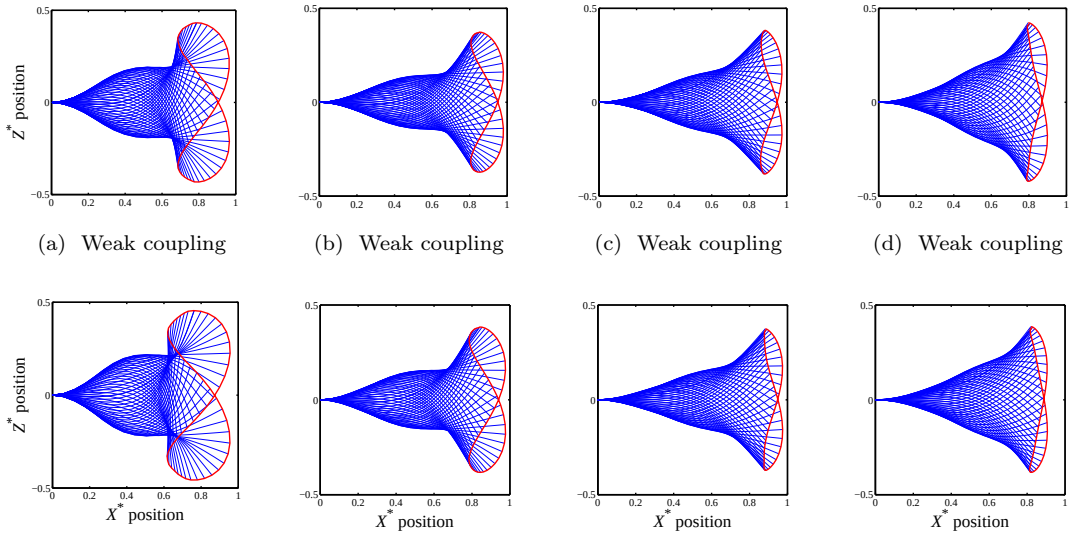

(a) Weak coupling (b) Weak coupling (c) Weak coupling (d) Weak coupling

(e) Strong coupling (f) Strong coupling (g) Strong coupling (h) Strong coupling

Figure 9: Behavior comparisons between the weak-coupling and proposed strong-coupling FSI analysis under (a)(e) $M^* = 0.4$, $U^* = 13$, $H^* = 1.0$, (b)(f) $M^* = 0.5$, $U^* = 15$, $H^* = 0.5$, (c)(g) $M^* = 1.0$, $U^* = 15$, $H^* = 0.3$, and (d)(h) $M^* = 1.5$, $U^* = 17$, $H^* = 0.2$.

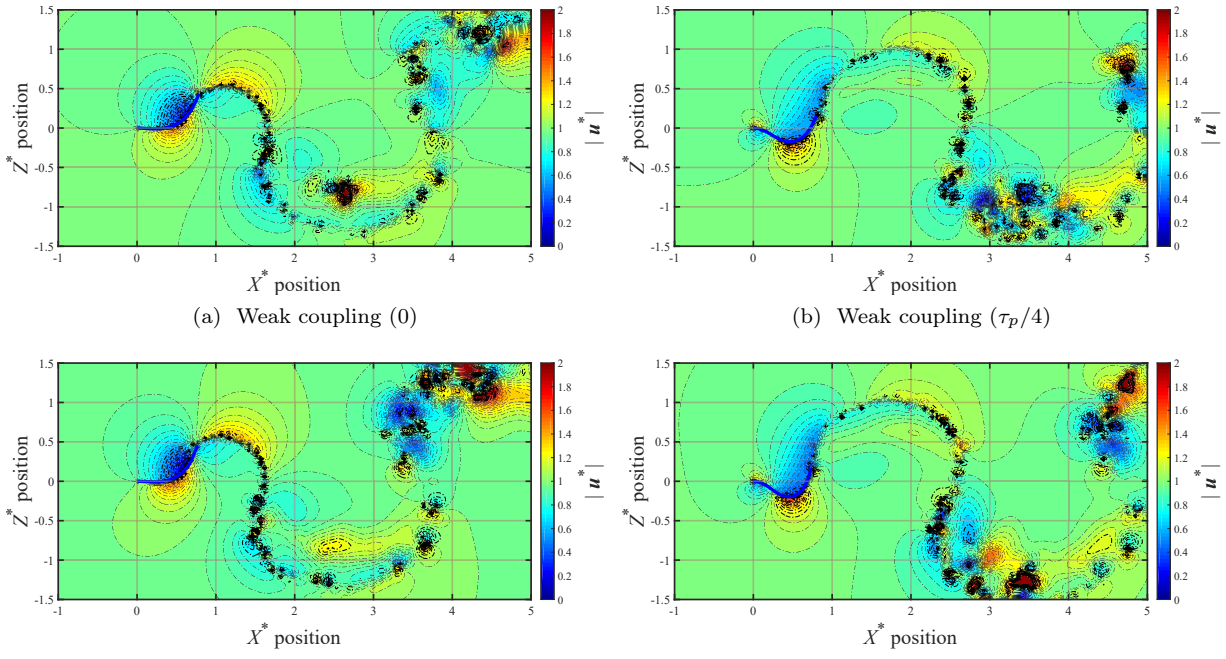

(a) Weak coupling (0) (b) Weak coupling ($\tau_p/4$)

(c) Strong coupling (0) (d) Strong coupling ($\tau_p/4$)

Figure 10: Velocity norm $|\boldsymbol{u}^*|$ distribution comparisons between the weak-coupling and proposed strong-coupling FSI analysis under $M^* = 0.4$, $U^* = 13$, $H^* = 1.0$.

coupled analysis, conditions were found in which the numerical analysis does not converge when the non-dimensional flow velocity U^* is large. Above mentioned problems are the potential future work.

Acknowledgment

This study was partially supported by a Grant-in-Aid for Scientific Research (C) (No.22K03983).

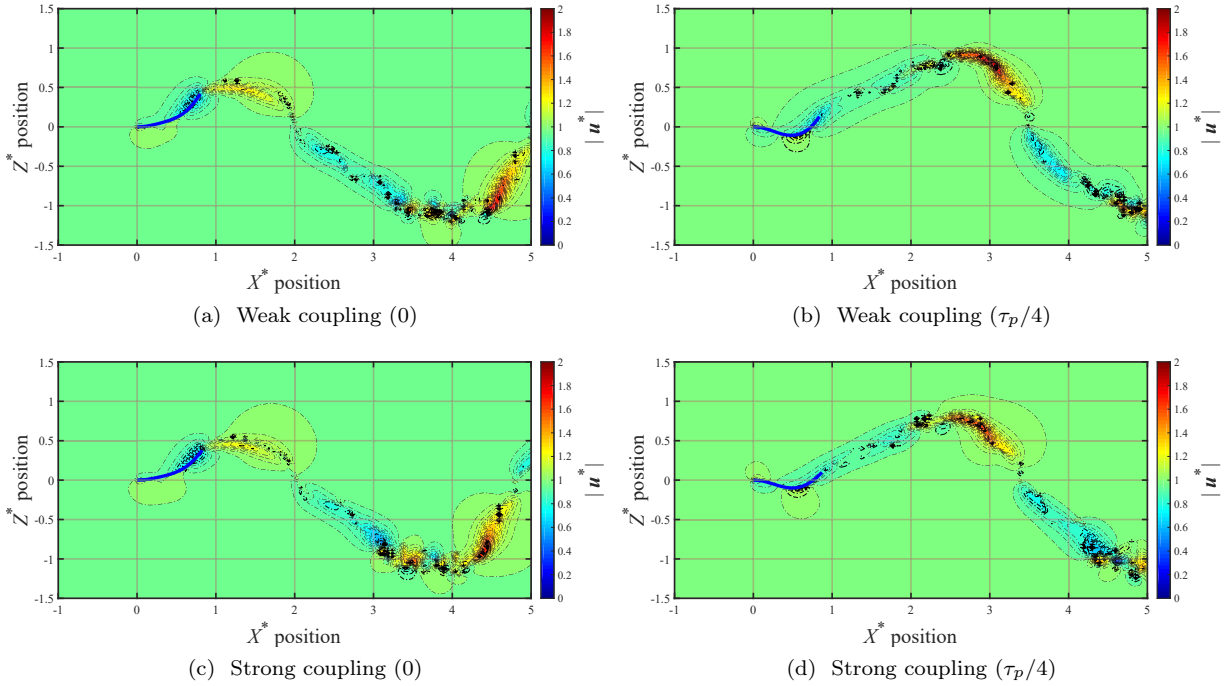

(a) Weak coupling (0)

(b) Weak coupling ($\tau_p/4$)

(c) Strong coupling (0)

(d) Strong coupling ($\tau_p/4$)

Figure 11: Velocity norm $|\boldsymbol{u}^*|$ distribution comparisons between the weak-coupling and proposed strong-coupling FSI analysis under $M^* = 1.5$, $U^* = 17$, $H^* = 0.2$.

References

[1] S. Michelin and O. Doaré. Energy harvesting efficiency of piezoelectric flags in axial flows. *Journal of Fluid Mechanics*, 714:489–504, 2013.

[2] S. Alben and M. J. Shelley. Flapping states of a flag in an inviscid fluid: Bistability and the transition to chaos. *Phys. Rev. Lett.*, 100:074301, Feb 2008.

[3] M. Chen, L. Jia, Y. Wu, X. Yin, and Y. Ma. Bifurcation and chaos of a flag in an inviscid flow. *Journal of Fluids and Structures*, 45:124–137, 2014.

[4] S. Michelin, S. Smith, and B. Glover. Vortex shedding model of a flapping flag. *Journal of Fluid Mechanics*, 617:1–10, 2008.

[5] T. Tezduyar, S. Sathe, R. Keedy, and K. Stein. Space–time finite element techniques for computation of fluid–structure interactions. *Computer Methods in Applied Mechanics and Engineering*, 195:2002–2027, 2006.

[6] T. Sawada and T. Hisada. Fluid-structure interaction analysis of the two-dimensional flag-in-wind problem by an interface-tracking ale finite element method. *Computers & Fluids*, 36(1):136–146, 2007.

[7] W. Huang and H. Sung. Three-dimensional simulation of a flapping flag in a uniform flow. *Journal of Fluid Mechanics*, 653(25):301–336, 2010.

[8] F. B. Tian, H. Luo, L. Zhu, and X. Y. Lu. Coupling modes of three filaments in side-by-side arrangement. *Physics of Fluids*, 23:1–14, 2011.

[9] J. Favier, A. Revell, and A. Pinelli. Numerical study of flapping filaments in au niform fluid flow. *Journal of Fluids and Structures*, 53:26–35, 2015.

[10] D. Dong, W. Chen, and S. Shi. Coupling motion and energy harvesting of two side-by-side flexible plates in a 3d uniform flow. *Applied Sciences*, 6(141):1–20, 2016.

[11] Y. Son and J. H. Lee. Flapping dynamics of coupled flexible flags in a uniform viscous flow. *Journal of Fluids and Structures*, 68:339–355, 2017.

[12] S. Olivieri, F. Viola, A. Mazzino, and M. Rosti. Direct numerical simulation of flapping flags in grid-induced turbulence. *Physics of Fluids*, 33:085116, 2021.

[13] A. Nawafleh, T. Xing, V. Durgesh, and R. Padilla. Fluid–structure interaction simulation of a flapping flag in a laminar jet. *Journal of Fluids and Structures*, 119:103869, 2023.

[14] A. Yamano, A. Shintani, T. Ito, C. Nakagawa, and H. Ijima. Influence of boundary conditions on a flutter-mill. *Journal of Sound and Vibration*, 478(21):1–14, 2020.

[15] A. Yamano, H. Ijima, A. Shintani, C. Nakagawa, and T. Ito. Influence of the aspect ratio of the sheet for an electric generator utilizing the rotation of a flapping sheet. *Mechanical Engineering Journal*, 8(1):1–15, 2021.
[16] J. Katz and A. Plotkin. *Low-speed Aerodynamics*. Cambridge University Press, 2001.
[17] T. Fritz and L. Long. Object-oriented unsteady vortex lattice method for flapping flight. *Journal of Aircraft*, 41(6):1275–1290, 2004.
[18] B. Stanford and P. Beran. Optimal thickness distributions of aeroelastic flapping shells. *Aerospace Science and Technology*, 24(1):116–127, 2013.
[19] A. Abdelkefi, M. Ghommem, A. Nuhait, and M. Hajj. Nonlinear analysis and enhancement of wing-based piezoaeroelastic energy harvesters. *Journal of Sound and Vibration*, 333(1):166–177, 2014.
[20] K. Dufva and A. Shabana. Analysis of thin plate structures using the absolute nodal coordinate formulation. *The Proceedings of the Institution of Mechanical Engineers, Part K: Journal of Multi-body Dynamics*, 219(4):345–355, 2005.
[21] A. Shabana. Computational continuum mechanics. *Chapter 6, Cambridge University Press*, pages 231–285, 2008.
[22] P. Hyldahl. Large displacement analysis of shell structures using the absolute nodal coordinate formulation. *Technical Reports Mechanical Engineering*, 6(2):1–38, 2013.
[23] P. Causin, J. Gerbeau, and F. Nobile. Added-mass effect in the design of partitioned algorithms for fluid–structure problems. *Computer Methods in Applied Mechanics and Engineering*, 194(42):4506–4527, 2005.
[24] N. Tsushima, T. Yokozeki, W. Su, and H. Arizono. Geometrically nonlinear static aeroelastic analysis of composite morphing wing with corrugated structures. *Aerospace Science and Technology*, 88:244–257, 2019.
[25] K. Otsuka, A. d. Carre, and R. Palacios. Nonlinear aeroelastic analysis of high-aspect-ratio wings with a low-order propeller model. *Journal of Aircraft*, 59(2):293–306, 2022.
[26] S. Chawdhury and G. Morgenthal. A partitioned solver to simulate large-displacement fluid–structure interaction of thin plate systems for vibration energy harvesting. *Computers & Structures*, 224:106110, 2019.
[27] L. Tang and M. Païdoussis. On the instability and the post-critical behaviour of two-dimensional cantilevered flexible plates in axial flow. *Journal of Sound and Vibration*, 305(1):97–115, 2007.
[28] L. Zhang, S. Zou, C. Wang, and J. Sun. A loosely-coupled scheme for the flow-induced flapping problem of two-dimensional flexible plate with strong added-mass effect. *Ocean Engineering*, 217:107656, 2020.
[29] D. Tang and E. H. Dowell. Aeroelastic response and energy harvesting from a cantilevered piezoelectric laminated plate. *Journal of Fluids and Structures*, 76:14–36, 2018.
[30] D. Tang, D. Levin, and E. H. Dowell. Experimental and theoretical correlations for energy harvesting from a large flapping flag response. *Journal of Fluids and Structures*, 86:290–315, 2019.
[31] T. Chen, M. Xu, D. Xie, and X. An. Post-flutter response of a flexible cantilever plate in low subsonic flows. *International Journal of Non-Linear Mechanics*, 91:113–127, 2017.
[32] M. Luo, Z. Wu, and C. Yang. Strongly coupled fluid–structure interaction analysis of aquatic flapping wings based on flexible multibody dynamics and the modified unsteady vortex lattice method. *Ocean Engineering*, 281:114921, 2023.
[33] A. Yamano and M. Chiba. Flow-induced vibration and energy-harvesting performance analysis for parallelized two flutter-mills considering span-wise plate deformation with geometrical nonlinearity and three-dimensional flow. *International Journal of Structural Stability and Dynamics*, 22(14):2250163, 2022.
[34] S. Michelin and S. G. L. Smith. Linear stability analysis of coupled parallel flexible plates in an axial flow. *Journal of Fluids and Structures*, 25(7):1136–1157, 2009.
[35] T. Theodorsen. General theory of aerodynamic instability and the mechanism of flutter. *National Advisory Committee for Aeronautics*, 496, 1934.
[36] D. Kumar, A. N. Arekar, and K. Poddar. The dynamics of flow-induced flutter of a thin flexible sheet. *Physics of Fluids*, 33(3):034131, 03 2021.